Published in final edited form as:
*Med Phys*. 2006 January ; 33(1): 216–224.

# Monte Carlo simulations of dose from microCT imaging procedures in a realistic mouse phantom

**Richard Taschereau**[a)], **Patrick L. Chow**, and **Arion F. Chatziioannou**
The Crump Institute for Molecular Imaging, Department of Molecular and Medical Pharmacology, University of California School of Medicine, 700 Westwood Boulevard, Los Angeles, California 90095

## Abstract

The purpose of this work was to calculate radiation dose and its organ distribution in a realistic mouse phantom from micro-computed tomography (microCT) imaging protocols. CT dose was calculated using GATE and a voxelized, realistic phantom. The x-ray photon energy spectra used in simulations were precalculated with GATE and validated against previously published data. The number of photons required per simulated experiments was determined by direct exposure measurements. Simulated experiments were performed for three types of beams and two types of mouse beds. Dose-volume histograms and dose percentiles were calculated for each organ. For a typical microCT screening examination with a reconstruction voxel size of 200 $\mu$m, the average whole body dose varied from 80 mGy (at 80 kVp) to 160 mGy (at 50 kVp), showing a strong dependence on beam hardness. The average dose to the bone marrow is close to the soft tissue average. However, due to dose nonuniformity and higher radiation sensitivity, 5% of the marrow would receive an effective dose about four times higher than the average. If CT is performed longitudinally, a significant radiation dose can be given. The total absorbed radiation dose is a function of milliamperes-second, beam hardness, and desired image quality (resolution, noise and contrast). To reduce dose, it would be advisable to use the hardest beam possible while maintaining an acceptable contrast in the image.

## I. INTRODUCTION

Micro-computed tomography (microCT) is a noninvasive investigation tool[1] among the imaging modalities available in small animal research. Utilizing x rays, it provides anatomical information and is used in a wide range of biological research studies: cancer, drug and other treatment effectiveness, bone micro architecture, myocardial microcirculation, and others.[1–6] The availability of small animal models—transgenic and knockout mice—contributes to the increased importance of microCT.[5]

The research subject animal receives non-negligible radiation dose during the procedure, which is primarily a function of the desired scan resolution, typically 50–200 $\mu$m, and noise level.[5,6] Special study protocols like respiratory and cardiac gated scans which require higher total photon flux can contribute to higher doses.[7] Other factors, like the number of scans (for longitudinal studies) and the concurrent use of positron emission tomography (PET) or single photon tomography (SPECT) can also contribute to increase the total dose received.[8,9]

a) rtaschereau@mednet.ucla.edu

Although the dose level is far from lethal, it might be high enough to cause biological effects that could interfere with the investigation. Several low-dose radiation effects have been reported[10–19] including effects on tumor growth and hematopoiesis. As microCT technology evolves rapidly, the limiting factor in high quality images will be most likely the x-ray dose administered.[20] Various suggestions for dose reduction have been made, for example by performing only half the scan around the subject.[21,22] However, they require the use of modified reconstruction algorithm limiting widespread applicability.

Most efforts in the field of small animal dosimetry so far have been oriented toward internal dosimetry. For example, Funk *et al.* have calculated the whole body dose in small animal from PET and SPECT isotopes in homogeneous ellipsoid phantoms of soft tissue from either a point source or a uniformly distributed source.[23] Geometrical phantoms are useful as first approximations of whole body dose, but more refinement is needed in order to assess potential biological effect. Another study, based on realistic anatomy from MRI, is from Kolbert *et al.*, who have used a point-kernel convolution method to calculate mouse-specific S factors for a few therapeutic radionuclides and a few organs.[24] Small animal CT dosimetry on the other hand has been little investigated. A study by Boone *et al.* provides tables to calculate whole body x-ray dose estimates from microCT[25] to a cylindrical mouse of homogeneous media. However, details of the spatial distribution of dose are not known.

The purpose of the Monte Carlo simulations in this work was to calculate detailed dosimetry, i.e., dose distributions on an organ basis in a realistic mouse phantom, from whole body microCT imaging protocols. By providing detailed data on the dose distribution in a series of organs and identifying regions receiving the highest dose, it is hoped that a better assessment of the potential biological effects and possible interference with biological studies will be achieved. It also provides valuable insight into ways to minimize dose.

## II. MATERIALS AND METHOD

This section is divided into five subsections briefly described here for clarity. In summary, in Sec. II A CT dose was calculated using GATE and in Sec. II B a voxelized, realistic phantom. The x-ray photon energy spectrum used in simulations was also calculated with GATE (Sec. II C). The number of photons required per simulated experiments was determined by direct exposure measurements (Sec. II D). Simulated experiments were performed for three types of x-ray beams and two types of beds (Sec. II E).

### A. Monte Carlo code

The GEANT4 Application for Tomographic Emission (GATE)[26] was used to perform all simulations. This software, which was initially developed for SPECT and PET tomograph development and imaging performance investigations, is based on the GEANT4[27] toolkit, a well-established and validated code for radiation transport.

The GATE script language allows for easy description of complex detector and phantom geometries. Detectors and phantoms can be portrayed with basic geometrical shapes and operations such as duplication along one or more axes or along a ring. More complex phantoms, such as the one used in this study, are best described with one or more matrices of voxels each having photon interaction properties. GATE keeps track of energy deposits in the phantom, calculates dose, and produces dose matrices having the same dimensions as the phantom.

GEANT4 and GATE come with an all-purpose set of physics processes and interaction models. However, for low energy applications such as medical physics and dose calculations, the low energy electromagnetic processes package is preferred (see

http://www.ge.infn.it/geant4/lowE/). The low energy package is an alternative to the standard physics processes that extends the validity range of particle interactions to lower energies (a few hundred electron volts to about 1 GeV). The package includes the photoelectric effect, Compton scattering, Rayleigh scattering, bremsstrahlung and ionization, while fluorescence from excited atoms is also treated.

### B. The realistic mouse phantom

The realistic mouse phantom used for simulations was an enhanced version of previously published work.[28] The phantom is a mathematical description of a 33 g mouse obtained from high-resolution magnetic resonance microscopy and can be realized as a voxelized phantom of any desired resolution, suitable for Monte Carlo experiments. For the whole organ portion of the present study, a $(400\ \mu m)^3$ voxel size and an 80×80×270 matrix were chosen as a compromise between resolution and computer resource consumption.

**1. Phantom enhancement—**The original mouse phantom lacked certain anatomical structures and did not possess tissue interaction property description. An enhanced phantom was created by adding new structures (skin, bladder wall, and bone marrow) and by segregating bone types (cranium, ribs, spines, and lower limbs) and air-containing organs (lungs, trachea, intestine).

New structures were made from contours created from selected parts of a binary version of the phantom. For example, the bladder wall was made from the contour of the original solid bladder—similarly for skin (contour of the whole phantom), bone marrow, and spine. Contours were produced by subtracting a smaller (eroded) version of the organ under consideration. Bone segregation was achieved according to their longitudinal position in the phantom. Figure 1 shows a cross section of the phantom before and after enhancement.

Each uniquely identified organ, tissue, or structure in the phantom was assigned a tissue composition, taken from their human counterparts and published in ICRU Report 46.[29] The bulk of the remainder of the mouse was described as a mixture of 80% muscle and 20% adipose tissue. Due to the relatively uniform soft tissue dose distribution, we do not anticipate that this approximation will have a significant impact on the produced results. Table I shows all 25 organs along with their tissue compositions.

**2. Bone marrow—**The high radiation sensitivity of bone marrow lead us to investigate the dose distribution in detail by using a high resolution $(15\ \mu m)^3$ voxel model of bone as shown in Fig. 2. The bone section, representative of the upper part of the femur, was about 2 mm in diameter and 1.5 mm in length. A layer of approximately 120 $\mu$m of cortical bone surrounded a pattern of trabecular bone and bone marrow cavities. Elemental compositions were taken from ICRU 46 definitions of skeleton-cortical bone (adult) and skeleton-spongiosa (adult).

### C. Photon spectra calculations

In order to efficiently simulate microCT procedures with the mouse phantom, photon energy spectra corresponding to peak voltages of 50, 70, and 80 kVp with 1, 2, and 3 mm of Al filtration (respectively) were precalculated with GATE. These voltage and filtration values are those actually used on our scanner and the calculation method is explained in the following paragraphs.

**1. Geometry—**A simplified geometry of the x-ray source of the Micro-CAT II scanner (Siemens Molecular Imaging, Knoxville, TN) was modeled. The x-ray source essentially consists of a tungsten enclosure (Fig. 3) housing an x-ray tube bathing in dielectric oil for

heat dissipation and having a thin carbon exit window. Beam filtration is achieved by placing aluminum disks of various thicknesses near the exit port.

The x-ray source block (model SB-80-250, Source-Ray Inc, Bohemia, NY) was described as a 1.4-cm-thick rectangular tungsten enclosure (5 cm×5 cm×11 cm). Located in the source block was a cylindrical x-ray tube (model PN 90507, Oxford Instruments, Scotts Valley, CA) bathing in dielectric oil having an estimated composition of $C_{12}H_8Cl_2$ and an estimated density of 0.885 g/cm$^3$. The tube dimensions were 8 cm long and 3 cm diameter and the tube glass thickness was 1.4 mm. The glass composition (in fractional mass) was: O (0.50), Si (0.32), Na (0.06), B (0.03), Al (0.03), Ba (0.02) and less than 1% of K, Ca, Z, Mg, and Fe. The anode target model was a tungsten cylinder (1.5 cm diameter, 1.5 cm long) tilted 20° with respect to the electron beam axis. The electron gun was modeled as a point source located 2 cm away from the center of the target. A 0.8-mm-thick carbon exit window (2 cm in diameter) was positioned in the enclosure at a distance of 2.6 mm from the x-ray tube. Beam filtration was achieved through a 4-cm-diam Al disk of 1, 2, or 3 mm in thickness.

**2. Spectrum calculation and validation—**Monoenergetic electrons were emitted from the electron gun onto the target with an energy corresponding to the peak voltage. Photon detection was achieved through an ideal detector made of a 1-cm-thick cylindrical tungsten plate of 20 cm in diameter. For each emitted electron in the x-ray source, the total energy deposited in the detector by bremsstrahlung photons and characteristic x rays was tallied and recorded in 1 keV energy increments, from 0 keV to the maximum energy (corresponding to the anode peak voltage). A total of $2{\cdot}10^9$ monoenergetic electrons were emitted toward the tungsten anode for each of the three simulated CT beams.

As a means to validate simulated spectra, a comparison has been made with previously published spectra.[30] The simulated spectrum of a 70 kVp beam (2 mm Al filtration) was compared to tabulated spectrum EM1 from Ref. [30]. To achieve agreement between Monte Carlo simulated and tabulated spectra, a total filtration of 2.7 mm Al was required for the tabulated spectrum. This implied that the total Al equivalent filtration of our simulated spectrum was also 2.7 mm Al. This value was consistent with the manufacturer's specifications. The two spectra shown in Fig. 4(a) have excellent agreement. The simulated spectrum possesses additional features such as characteristic x rays and *K* edge absorption from Ba (present in the tube glass) at around 32 and 37 keV, respectively. All three simulated spectra, shown in Fig. 4(b), are subsequently used to emit photons in CT procedure simulations. The result is computationally efficient Monte Carlo simulations with accurate x-ray beam characteristics.

### D. Determination of the number of photons required by simulations

A value of utmost importance for absolute dose calculations with Monte Carlo simulations was the number of photons to track in order to reproduce an experiment. This value, which can be expressed as a photon flux (photons per unit solid angle per unit current per second), could be estimated in a number of ways.

An estimate could be made analytically from the entire sequence of events from electron emission in the tube down to energy deposition in the phantom or ionization chamber. However, due to the number of phenomena involved and the complexity of the geometry, such an estimate would entail considerable uncertainty. A second and possibly less uncertain approach would be to still use an analytical approach, but to start later in the chain of events and use the photon energy spectrum of the source to calculate energy deposition. A third approach would be to use Monte Carlo to simulate measurements in the beam with an ionization chamber and, by comparison to measurements, directly obtain a correspondence factor.

In this study, the last two methods have been used: the Monte Carlo-measurements method as the principal source and the analytical method as a cross-verification. Since both approaches are based on measurements made with an ionization chamber, the measurement procedure is described first. Then follows a more detailed description of the two calculation methods and a discussion.

**1. Exposure measurements—**Exposure measurements at the center of the x-ray beam were performed with a 10-cm-long CT ionization chamber (10X5-3CT Special, Radcal Corporation, Monrovia, CA). The chamber had an inner diameter of 6.4 mm and a volume of 3 $cm^3$ and was located at the isocenter at a distance of 21.8 cm from the source focal point. An average exposure was obtained from a set of ten individual exposures of 0.5 s with a current of 0.5 mA. Electrometer readings were corrected for energy, temperature, and pressure. The x-ray tube voltage was set to 50, 70, and 80 kVp and the average corrected readings were: 7.38, 6.34, and 6.26 $\mu$C/kg respectively.

**2. Estimation from Monte Carlo and measurements—**This estimation method was straightforward. A Monte Carlo simulation of the dose deposited in air at the isocenter was performed by following $10^9$ photon histories having energies in accordance with the precalculated photon spectrum. Calibration factors $f_c$, shown in Table II (line 4), were subsequently calculated by dividing the mGy/mA s value obtained with measurements by the value obtained with simulations:

$$f_c = \frac{(\text{mGy/mA s})_{\text{measured}}}{(\text{mGy/photons})_{\text{simulated}}}.$$

**3. Analytical estimation—**With this method, we estimated the photon flux at the center of the scanner from the total energy deposited in the ion chamber and an average energy deposit per photon derived from analytical expressions. For a given irradiation, characterized by duration and an x-ray tube current, the exposure reading from the electrometer was readily converted to the total energy deposited in the ion chamber using the following expression:

$$E_{\text{tot}} = X \cdot W \cdot \rho_{\text{air}} \cdot V_{\text{chamber}} \quad (1)$$

where $X$ was the exposure reading in C/kg and $W$ was the average energy required to produce one ion pair in dry air (33.97 J/C). Dividing $E_{\text{tot}}$ by the spectrum-weighted average energy deposited per photon $\bar{E}_{\text{dep}}$, by the solid angle $\Omega$ subtended by the chamber and by the current-time product (mA s) of the x-ray tube, we obtained the number of photons per steradian per millampere per second:

$$\Phi = \frac{E_{\text{tot}}}{\bar{E}_{\text{dep}} \cdot \Omega \cdot \text{mA s}}. \quad (2)$$

We now calculate $\bar{E}_{\text{dep}}$, the average energy deposited per photon. Assuming radiative loss was negligible, the energy-dependent average energy deposit $E_{\text{dep}}(E)$ of a photon of energy $E$ passing through the thickness $x$ of air (the average cord length through the chamber section) was calculated with the mass energy-absorption coefficient $\mu_{\text{en}}/\rho$ at energy $E$:

$$E_{\text{dep}}(E) = E \cdot (1 - e^{(\mu_{en}/\rho)(E) \cdot \rho_{\text{air}} \cdot x}). \quad (3)$$

The spectrum-weighted average energy deposited per photon $\bar{E}_{dep}$ is a function of the energy spectrum of the photon beam $n(E)dE$. However, since the beam was already attenuated by a thickness of air before reaching the ion chamber, an attenuated spectrum $n'(E)dE$ was used and was defined as follows:

$$n'(E)dE = \frac{e^{(\mu/\rho)(E)\rho_{air}SIC} \cdot n(E)dE}{\int e^{(\mu/\rho)(E)\rho_{air}SIC} \cdot n(E)dE}, \quad (4)$$

where $n(E)dE$ was the unattenuated spectrum and SIC was the source-to-isocenter distance (21.8 cm). Finally, $\bar{E}_{dep}$ was calculated combining Eqs. (3) and (4):

$$\overline{E}_{dep} = \int \overline{E}_{dep}(E) \cdot n'(E)dE. \quad (5)$$

The parameters and values obtained with the precalculated spectra and Eqs. (1)–(5) are shown in Table III.

**4. Comparison—**A comparison of the number of photon histories required to simulate 1 mA s obtained by the analytical and Monte Carlo methods shows a difference of about 6%, 9%, and 12% for beams at 50, 70, and 80 kVp, respectively. Considering the simplifications of the analytical approach, e.g., scatter not taken into account, it agrees reasonably well with the empirical approach and gives confidence in Monte Carlo results. Hence, the values used for phantom simulations in this study are those found by Monte Carlo and shown in Table II.

It is of interest to note that an upward trend was observed in calibration factors with both calculation methods (Monte Carlo-measurements method, Table II, line 4 and analytical method, Table III, line 5). This was due to the combined effect of increased bremsstrahlung photon production efficiency and decreased Al filtration as peak voltage increases. In other words, for the same tube current more photons were present in the beam. As a consequence, more photons per mA s have to be simulated for higher peak voltage beams.

## E. CT Procedures

**1. Protocols—**The total mA s values routinely used per CT acquisitions in practice vary according to peak voltage. These values were chosen by the CT system manufacturer to provide approximately the same amount of charge collected in the CCD camera (60% of the maximum in a 12-bit digitizer). At 70 kVp, a typical screening protocol calls for 360 exposures of 0.5 s each, at one degree interval with a tube current of 0.5 mA (90 mA s total). For 50 and 80 kVp, 162 (0.5 mA ×0.9 s×360 views) and 81 (0.5 mA×0.45 s×360 views) mA s were used, respectively.

CT procedures were simulated for six imaging scenarios combining the three precalculated x-ray beams and two mouse holder arrangements: our custom made PMMA bed system[31] and the microCT manufacturer's carbon fiber bed.

**2. Geometry—**The PMMA bed (monomer composition $C_5O_2H_8$) consisted of a sled on which the mouse rests contained in a cylindrical enclosure fully covering the mouse. The sled was 1.5 mm thick, 16 cm long, and spanned an arc of 90° on a 23.9 mm (inner) radius circle. The outer cylindrical enclosure was also 1.5 mm thick, was 19 cm long, and had an inner radius of 21 mm.

The carbon fiber bed, which does not cover but only supports the mouse, was 1 mm thick, 20 cm long, and spanned an arc of 135° on a 23.4 mm (inner) radius circle. Its composition

is proprietary but was estimated as a mixture of the following fractional mass composition: C(0.968), O(0.0233), and H(0.0087), with a density of 1.8 g/cm$^3$ to account for an organic resin mixed with carbon fibers.

Photons were issued according to precalculated energy spectra in a cone beam of 12.95° (half angle). Although the actual x-ray source has a half angle of 20°, lead collimators in the CT gantry narrow the beam to 12.95° so that it just covers the detector area. All photons were tracked down to zero energy, as there is no tracking cut in GEANT, only particle production cut. The x-ray source was located at a distance of 218 mm from the isocenter (the SIC distance of the microCAT II) where the mouse was located.

**3. Dose scaling—**For each of the six simulated imaging protocols a total of $2.4 \cdot 10^9$ photons were tracked, covering 120 exposures angles of $2 \cdot 10^7$ photons per angle simulating a 360° circle with 3° increments. Energy deposited from photons and electrons was tallied for each voxel and radiation dose was calculated by dividing the total energy deposited by the voxel mass. Relative uncertainty on dose per voxel was calculated by GATE as the ratio of the standard error of the mean over the mean itself (for a detailed description of the calculations, the reader is referred to the GATE User's Manual). The average uncertainty per voxel was around 5% and the overall uncertainty on the average dose per organ was better than 3% (this is for the thyroid, the smallest organ: 0.016 mm$^3$). Since the number of simulated photons was orders of magnitude less than the number of photons in actual CT examinations, the calculated dose had to be scaled up with the appropriate calibration factor to the mA s level of the procedure. For example, at 70 kVp a 90 mA s procedure would require 90 mA s×$1.45 \cdot 10^{11}$ photons/mA s=$1.3 \cdot 10^{13}$ photons to be simulated. The scaling factor used in this case was $1.3 \cdot 10^{13}$ x-ray photons/$2.4 \cdot 10^9$ simulated photons = 5437. Each simulation took about 1000 h of processor time to complete and was run under the Linux Operating system on a cluster of dual 3.2-GHz xeon processors each having 4 Gbytes of memory installed.

In addition to these simulations, one low noise simulation for the 70 kVp/2 mm Al beam with the PMMA bed was computed, allowing for the calculation of dose-volume histograms on a per voxel basis. The simulation tracked $7.2 \cdot 10^9$ photon histories to give an uncertainty of 5% or better on 90% of the voxels.

For simulations with the bone marrow phantom, efficiency was increased by reducing the half-angle of the x-ray cone beam from its nominal value of 12.95° to 0.3°, enough to cover only the simulated bone segment. Because of the very small angle, it was possible to simulate the actual microCT flux by tracking only $7 \cdot 10^9$ photons. However, there was less soft tissue surrounding the bone in the (smaller) bone phantom than in the full mouse phantom with the consequence that an artificially higher dose was calculated because of the smaller attenuation. To compensate for that artifact, all dose values calculated with the bone phantom were scaled down by multiplication with a scaling factor of 0.947. This value was obtained from the ratio of dose to soft tissue in the full phantom over dose to soft tissue section surrounding the bone phantom.

## III. RESULTS AND DISCUSSION

### A. Bone and soft tissue

Table IV shows in ascending order of average dose, the dose average and 95th percentile of the dose distribution in most organs for the 70 kVp/2 mm Al beam with custom PMMA bed system. Table IV presents absolute dose for a 90 mA s examination and relative dose with respect to air kerma measured at the isocenter. The ratio of the 95th percentile over the average helps appreciate the length of the tail of the dose distribution, in other words how

representative is the dose average. Omitted in that list are the contents of hollow structures such as the trachea, and water filled structures such as the stomach, bladder, and intestine since dose to air or water is irrelevant. However, all structures were considered for the purpose of photon tracking. The average dose ranges from 71 mGy (spine marrow) to about 400 mGy (cranium). It can be readily seen that bony structures received the highest dose (230–400 mGy) while soft tissue received lower and more homogeneous dose (70–90 mGy). The spine marrow received the lowest dose because of the protection provided by the spinal cord. Dose distributions per organ were relatively uniform as can be seen from the 95th percentile, which is about 10% above the average in most cases. The most inhomogeneous distributions were observed in the lower limbs (36%) and in the skin (19%). The whole body (all organs) dose average was 93 mGy. However, the dose distribution was nonuniform since the 95th percentile was almost three times the average. Since dose is additive, the dose distribution in the phantom is scalable and dose ratios for a given beam, e.g., heart dose/whole body dose and 95th percentile/average remain unchanged regardless of the total number of mA s used for the scan.

Calculated dose values can be compared to published data. The air kerma measured at our SIC distance (21.8 cm) was 0.8608 mGy per mA s, or 77.47 mGy kerma for a typical 90 mAs-CT. According to Table IV in Ref. [25], for a beam of 70 kVp with 2 mm Al added filtration, a 30-cm SIC and a 30-mm-diam mouse, the dose/kerma ratio is 0.8716, which yields an average dose to the mouse of 128 mGy (after correcting for distance).

This value is higher than the 93 mGy calculated in this study, however this can be considered in relatively good agreement especially taking into account the simplified approach used in Ref. [25]. The difference between the two studies could be explained by beam hardness. For example, our simulations take into account the fact that the mouse is actually supported by a PMMA bed and is not suspended in air, which will contribute to increased hardness. There is also some uncertainty in the inherent filtration of x-ray tubes that can be up to a couple mm Al. The lower value observed in this study suggests that the beam used is harder than the one used in Ref. [25].

Figure 5 shows a differential dose-volume histogram of the fractional volume density (in $mGy^{-1}$) from the low noise CT simulation with the PMMA bed and a 70 kVp/2 mm Al beam. The dashed line represents bony structures (ribs, spine bone, cranium, and limbs) while the solid curve represents bulk background soft tissue (all others in Table IV). Dose to soft tissue has a narrow distribution (more homogeneous dose) around 80 mGy while the dose to bones is more spread out and can be quite high (e.g., >400 mGy for parts of the cranium). The nonzero portion of both curves near 10 mGy is due to the posterior extremity of the mouse at the edge of the field of view that receives almost no x-rays.

Spatial and statistical dose distributions in bone marrow from the high-resolution bone phantom are shown in Fig. 6. Figure 6(a) shows a cross section of the dose image. In each marrow cavity, dose is relatively uniform and is mostly due to interacting photons in marrow itself. However, the highest dose is systematically found in the periphery of these cavities. A dose-volume histogram is shown in Fig. 6(b). The fine spatial resolution reveals a slightly skewed distribution: the 95th dose percentile is 114 mGy and the 99th percentile is 138 mGy.

It is also worth mentioning that other protocols can give very different dose averages. However, it is easy to scale dose according to the total mA s used. For example, a “low resolution” protocol used solely for PET/SPECT attenuation corrections would typically be about one-tenth (8 mA s) of the normal protocol giving also one-tenth of the dose.

### B. Beam and mouse holder

The average dose to selected organs—including the body as a whole—is shown in Fig. 7. Dose values are plotted for x-ray beams of 50, 70, and 80 kVp with 1, 2, and 3 mm Al filters, respectively, and the two mouse holders (PMMA and carbon fiber). With both holders, the average dose decreases with increasing beam energy (this is especially noticeable with bones). The most important difference is observed between 80 and 50 kVp where the average dose is 50% lower depending on the organ (more pronounced with bones). This is due to a lower mA s value used but also because less energy is deposited, the attenuation coefficient becoming smaller with energy. The dose differential (as well as imaging contrast) also decreases with increasing energy. The average dose is slightly lower (1–3%) with the PMMA bed because, by covering the mouse all around, it provides more low-energy photon filtration compared to the carbon fiber bed. The phenomenon is more noticeable at 50 kVp.

## IV. CONCLUSION

In this study, Monte Carlo simulations were used to calculate the radiation dose received by individual organs of a mouse subjected to microCT imaging procedures. Two mouse holder configurations as well as three beam qualities were investigated.

For a typical microCT examination, the average whole body dose varied from 80 mGy (at 80 kVp) to 160 mGy (at 50 kVp). If CT is combined with other radiological imaging modalities, an important radiation dose can be given. As an example, a series of 5 PET and CT scans at 50 kVp would give a body average of 800 mGy from the CT scans alone, on top of which the PET dose (tens of mGy per scan[23]) would be added. The total average dose would be above 1 Gy. The significance of this dose may be appreciated by comparing it to the LD50/30[32] for mice estimated at about 7 Gy, although the LD50/30 is for a single, acute radiation dose, as opposed to the fractionated dose of a series of scans. The average dose to the bone marrow is close to the soft tissue average. However, the dose distribution is inhomogeneous as shown by the 95th percentile (30% higher than the average). If the sensitivity of the bone marrow is two to three times that of soft tissue (as in humans[33]), then a fraction (5%) of the marrow would receive an effective dose about four times higher than the average.

The total absorbed radiation dose is a function of the number of scans, mA s per scan, beam hardness, and desired image quality (resolution, noise and contrast). To reduce dose, it would then be advisable to use the hardest beam possible while maintaining an acceptable contrast in the image. Imaging protocols combining other modalities to which the CT is only used as a reference can safely reduce the resolution and dose from the CT protocols by large factors.[20,34]

## Acknowledgments

The authors wish to thank R. Scott Beach and Shaun S. Gleason from Siemens-CTI for providing information regarding the scanner and the bed, Paul Sunde from Radcal Corporation for calibrating the ion chamber, David Stout for scheduling scanner time, an d Judy Edwards, Waldemar Ladno, and Victor Dominguez for their assistance in setting up the microCT scanner. This work was supported in part by the U.S. Department of Energy under Contract No. DE-FC03 02ER63420 and by the National Institutes of Health under Grant No. R24 CA92865.

## References

1. De Clerck NM, Meurrens K, Weiler H, Van Dyck D, Vanhoutte G, Terpstra P, Postnov AA. High-resolution x-ray microtomography for the detection of lung tumors in living mice. Neoplasia 2004;6:374–379. [PubMed: 15256059]

2. Ding M, Odgaard A, Hvid I. Changes in the three-dimensional microstructure of human tibial cancellous bone in early osteoarthritis. J Bone Jt Surg, Br 2003;85B:906–912.

3. Hildebrandt IJ, Gambhir SS. Molecular imaging applications for immunology. Clin Immunol 2004;111:210–224. [PubMed: 15137954]

4. Malyar NM, Gossl M, Beighley PE, Ritman EL. Relationship between arterial diameter and perfused tissue volume in myocardial microcirculation: A microCT-based analysis. Am J Physiol Heart Circ Physiol 2004;286:H2386–H2392. [PubMed: 14670815]

5. Paulus MJ, Gleason SS, Kennel SJ, Hunsicker PR, Johnson DK. High resolution x-ray computed tomography: An emerging tool for small animal cancer research. Neoplasia 2000;2:62–70. [PubMed: 10933069]

6. Ritman EL. Micro-computed tomography-current status and developments. Annu Rev Biomed Eng 2004;6:185–208. [PubMed: 15255767]

7. Badea C, Hedlund LW, Johnson GA. MicroCT with respiratory and cardiac gating. Med Phys 2004;31:3324–3329. [PubMed: 15651615]

8. Berger F, Lee YP, Loening AM, Chatziioannou A, Freedland SJ, Leahy R, Lieberman JR, Belldegrun AS, Sawyers CL, Gambhir SS. Whole-body skeletal imaging in mice utilizing microPET: Optimization of reproducibility and applications in animal models of bone disease. Eur J Nucl Med Mol Imaging 2002;29:1225–1236. [PubMed: 12418463]

9. Chow PL, Rannou FR, Chatziioannou AF. Attenuation correction for small animal PET tomographs. Phys Med Biol 2005;50:1837–1850. [PubMed: 15815099]

10. Chen SL, Cai L, Meng QY, Xu S, Wan H, Liu SZ. Low-dose whole-body irradiation (LD-WBI) changes protein expression of mouse thymocytes: Effect of a LD-WBI-enhanced protein RIP10 on cell proliferation and spontaneous or radiation-induced thymocyte apoptosis. Toxicol Sci 2000;55:97–106. [PubMed: 10788564]

11. Li W, Wang GJ, Cui JW, Xue L, Cai L. Low-dose radiation (LDR) induces hematopoietic hormesis: LDR-induced mobilization of hematopoietic progenitor cells into peripheral blood circulation. Exp Hematol 2004;32:1088–1096. [PubMed: 15539087]

12. Liu SZ. On radiation hormesis expressed in the immune system. Crit Rev Toxicol 2003;33:431–441. [PubMed: 12809432]

13. Mitchel REJ, Jackson JS, Morrison DP, Carlisle SM. Low doses of radiation increase the latency of spontaneous lymphomas and spinal osteosarcomas in cancer-prone, radiation-sensitive Trp53 heterozygous mice. Radiat Res 2003;159:320–327. [PubMed: 12600234]

14. Prise KM, Folkard M, Michael BD. A review of the bystander effect and its implications for low-dose exposure. Radiat Prot Dosimetry 2003;104:347–355. [PubMed: 14579891]

15. Schettino G, Folkard M, Michael BD, Prise KM. Low-dose binary behavior of bystander cell killing after microbeam irradiation of a single cell with focused C-K x rays. Radiat Res 2005;163:332–336. [PubMed: 15733040]

16. Silasi G, Diaz-Heijtz R, Besplug J, Rodriguez-Juarez R, Titov V, Kolb B, Kovalchuk O. Selective brain responses to acute and chronic low-dose x ray irradiation in males and females. Biochem Biophys Res Commun 2004;325:1223–1235. [PubMed: 15555557]

17. Ulsh BA, Miller SM, Mallory FF, Mitchel REJ, Morrison DP, Boreham DR. Cytogenetic dose-response, and adaptive response in cells of ungulate species exposed to ionizing radiation. J Environ Radioact 2004;74:73–81. [PubMed: 15063537]

18. Wan H, Gong SL, Liu SZ. Effects of low dose radiation on signal transduction of neurons in mouse hypothalamus. Biomed Environ Sci 2001;14:248–255. [PubMed: 11723726]

19. Yu HS, Song AQ, Lu YD, Qui WS, Shen FZ. Effects of low-dose radiation on tumor growth, erythrocyte immune function and SOD activity in tumor-bearing mice. Chin J Physiol 2004;117:1036–1039.

20. Ford NL, Thornton MM, Holdsworth DW. Fundamental image quality limits for microcomputed tomography in small animals. Med Phys 2003;30:2869–2877. [PubMed: 14655933]

21. Liu Y, Liu H, Wang Y, Wang G. Half-scan cone-beam CT fluoroscopy with multiple x-ray sources. Med Phys 2001;28:1466–1471. [PubMed: 11488580]

22. Yu LF, Pan XC. Half-scan fan-beam computed tomography with improved noise and resolution properties. Med Phys 2003;30:2629–2637. [PubMed: 14596299]

23. Funk T, Sun MS, Hasegawa BH. Radiation dose estimate in small animal SPECT and PET. Med Phys 2004;31:2680–2686. [PubMed: 15487751]
24. Kolbert KS, Watson T, Matei C, Xu S, Koutcher JA, Sgouros G. Murine S factors for liver, spleen, and kidney. J Nucl Med 2003;44:784–791. [PubMed: 12732681]
25. Boone JM, Velazquez O, Cherry SR. Small-animal x ray dose from microCT. Molecular Imaging 2004;3:149–158. [PubMed: 15530250]
26. Jan S, Santin G, Strul D, Staelens S, Assie K, Autret D, Avner S, Barbier R, Bardies M, Bloomfield PM, Brasse D, Breton V, Bruyndonckx P, Buvat I, Chatziioannou AF, Choi Y, Chung YH, Comtat C, Donnarieix D, Ferrer L, Glick SJ, Groiselle CJ, Guez D, Honore PF, Kerhoas-Cavata S, Kirov AS, Kohli V, Koole M, Krieguer M, van der Laan DJ, Lamare F, Largeron G, Lartizien C, Lazaro D, Maas MC, Maigne L, Mayet F, Melot F, Merheb C, Pennacchio E, Perez J, Pietrzyk U, Rannou FR, Rey M, Schaart DR, Schmidtlein CR, Simon L, Song TY, Vieira JM, Visvikis D, Van de Walle R, Wieers E, Morel C. GATE: A simulation toolkit for PET and SPECT. Phys Med Biol 2004;49:4543–4561. [PubMed: 15552416]
27. Agostinelli S, Allison J, Amako K, Apostolakis J, Araujo H, Arce P, Asai M, Axen D, Banerjee S, Barrand G, Behner F, Bellagamba L, Boudreau J, Broglia L, Brunengo A, Burkhardt H, Chauvie S, Chuma J, Chytracek R, Cooperman G, Cosmo G, Degtyarenko P, Dell'Acqua A, Depaola G, Dietrich D, Enami R, Feliciello A, Ferguson C, Fesefeldt H, Folger G, Foppiano F, Forti A, Garelli S, Giani S, Giannitrapani R, Gibin D, Cadenas JJG, Gonzalez I, Abril GG, Greeniaus G, Greiner W, Grichine V, Grossheim A, Guatelli S, Gumplinger P, Hamatsu R, Hashimoto K, Hasui H, Heikkinen A, Howard A, Ivanchenko V, Johnson A, Jones FW, Kallenbach J, Kanaya N, Kawabata M, Kawabata Y, Kawaguti M, Kelner S, Kent P, Kimura A, Kodama T, Kokoulin R, Kossov M, Kurashige H, Lamanna E, Lampen T, Lara V, Lefebure V, Lei F, Liendl M, Lockman W, Longo F, Magni S, Maire M, Medernach E, Minamimoto K, de Freitas PM, Morita Y, Murakami K, Nagamatu M, Nartallo R, Nieminen P, Nishimura T, Ohtsubo K, Okamura M, O'Neale S, Oohata Y, Paech K, Perl J, Pfeiffer A, Pia MG, Ranjard F, Rybin A, Sadilov S, Di Salvo E, Santin G, Sasaki T, Savvas N, Sawada Y, Scherer S, Seil S, Sirotenko V, Smith D, Starkov N, Stoecker H, Sulkimo J, Takahata M, Tanaka S, Tcherniaev E, Tehrani ES, Tropeano M, Truscott P, Uno H, Urban L, Urban P, Verderi M, Walkden A, Wander W, Weber H, Wellisch JP, Wenaus T, Williams DC, Wright D, Yamada T, Yoshida H, Zschiesche D. Geant4-a Simulation Toolkit. Nucl Instrum Methods Phys Res A 2003;506:250–303.
28. Segars WP, Tsui BMW, Frey EC, Johnson GA, Berr SS. Development of a 4-D digital mouse phantom for molecular imaging research. Mol Imaging Biol 2004;6:149–159. [PubMed: 15193249]
29. ICRU Report 46. International Commission on Radiation Units and Measurements; Bethesda, MD: 1992. Photon, electron, proton, and neutron interaction data for body tissues.
30. Fewell, TR.; Shuping, RE.; Hawkins, KR. Handbook of Computed Tomography X-ray Spectra. U.S. Deptartment of Health and Human Services, Public Health Service, Food and Drug Administration, Bureau of Radiological Health; Rockville, MD: 1981. United States. Bureau of Radiological Health, and United States. Bureau of Radiological Health. Division of Electronic Products; p. vip. 101
31. Stout DB, Chow PL, Gustilo A, Grubwieser S, Chatziioannou AF. Multimodality isolated bed system for mouse imaging experiments. Mol Imaging Biol 2003;5:128–129.
32. Samarth RM, Kumar A. Radioprotection of Swiss albino mice by plant extract Mentha piperita (Linn.). J Radiat Res (Tokyo) (Tokyo) 2003;44:101–109.
33. ICRP Publications. Pergamon Press; Oxford, New York: 1991. 1990 Recommendations of the International Commission on Radiological Protection - Users' Edition, 60; p. 215
34. Chow PL, Rannou FR, Chatziioannou AF. Towards a beam hardening correction for a microCT scanner. Molecular Imaging 2004;6:77–78.

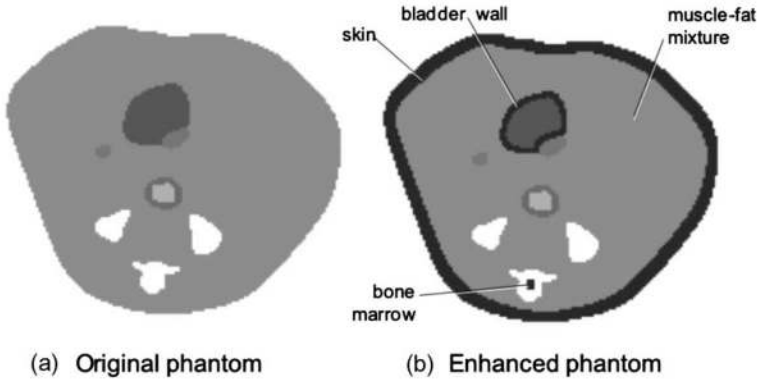


**Fig. 1.**
Transverse slice of (a) the original mouse phantom, and (b) the enhanced phantom. The added structures (skin, bladder wall, muscle-fat mixture, and bone marrow) have been identified.

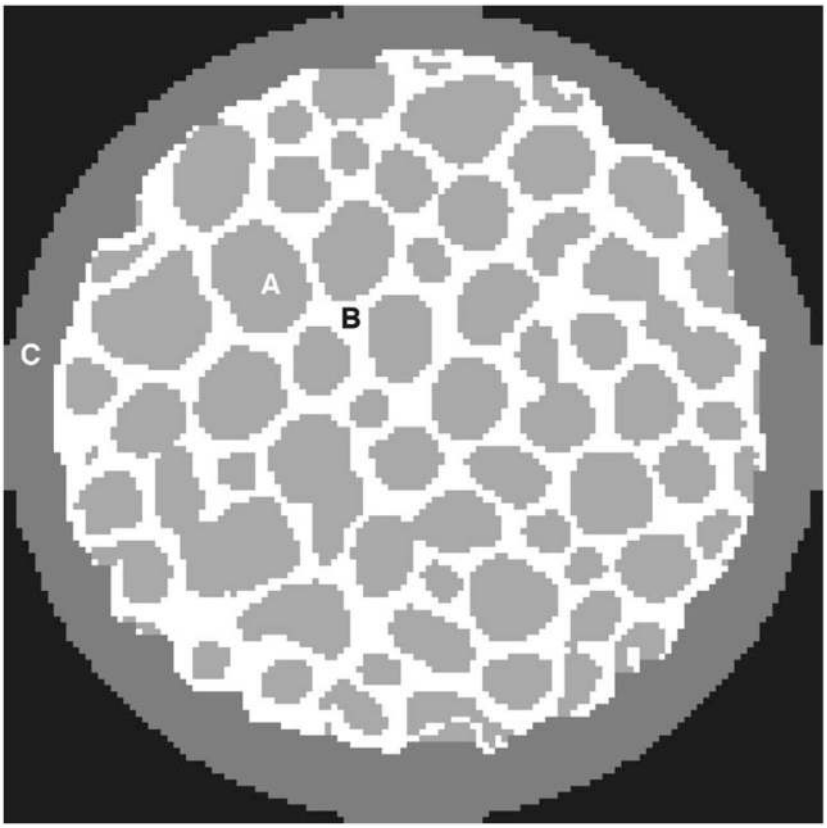


**Fig. 2.**
Cross section of the high resolution (15 $\mu$m)$^3$/voxel bone phantom showing (a) the bone marrow, (b) trabecular bone, and (c) cortical bone.

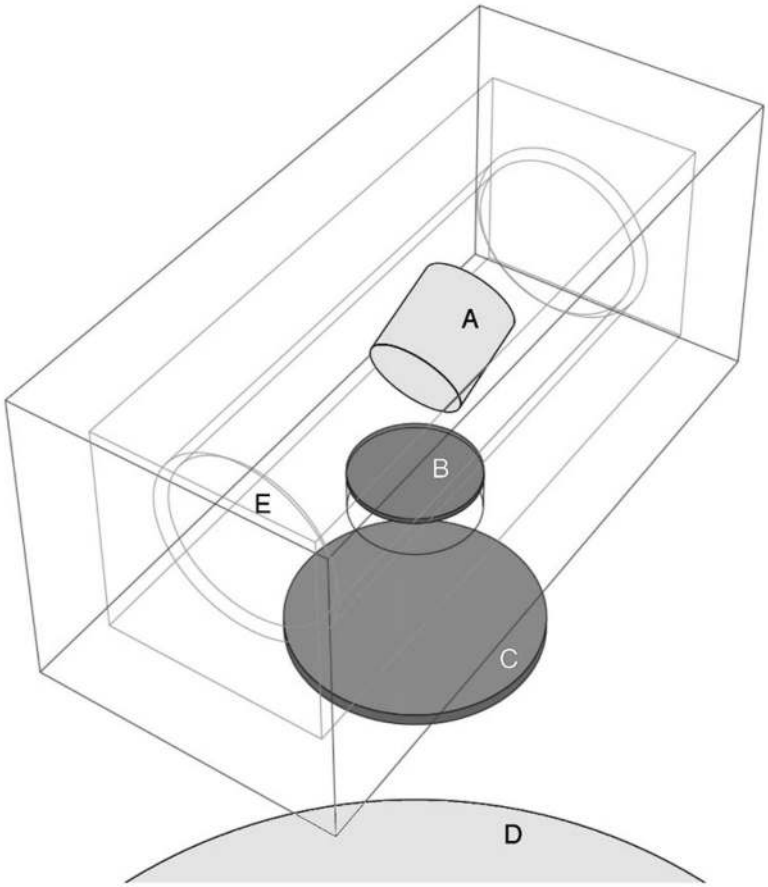


**Fig. 3.**
X-ray source geometry used in calculating photon energy spectra: (a) tungsten anode (target), (b) exit window, (c) aluminum filter, (d) detector, and (e) location of the electron gun (a point source).

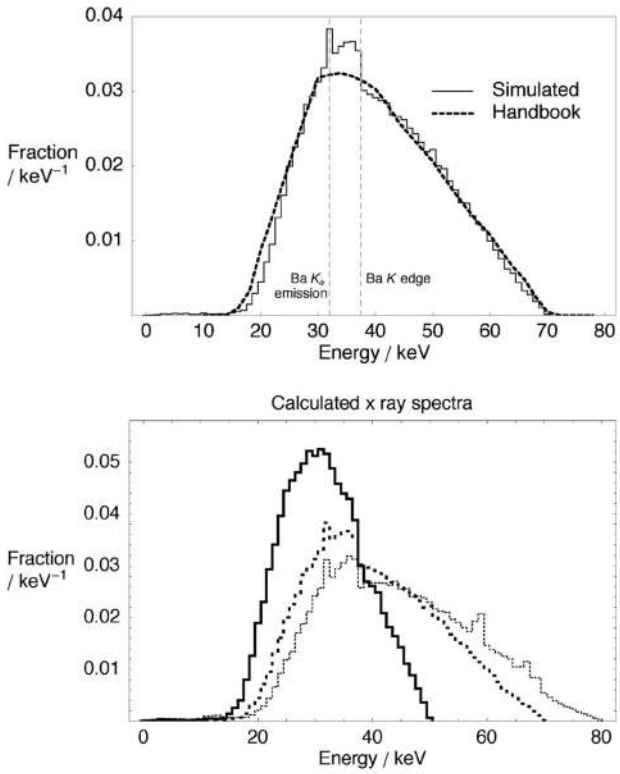


**Fig. 4.**

(a) Comparison of the GATE-calculated x-ray spectra at 70 kVp (solid line) and a tabulated spectra from Ref. [30] (dashed line), and (b) calculated x-ray spectra at three energies: 50 kVp/1 mm Al (thick solid line); 70 kVp/2 mm Al (thick dashed), and 80 kVp/3 mm Al (thin dashed).

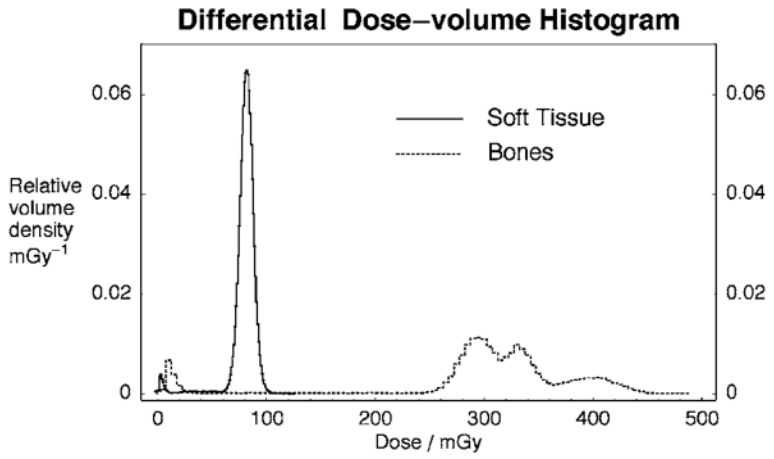


**Fig. 5.**

Differential dose-volume histogram obtained at 70 kVp with 2 mm Al filtration for soft tissue (solid line) and bones (dashed line).

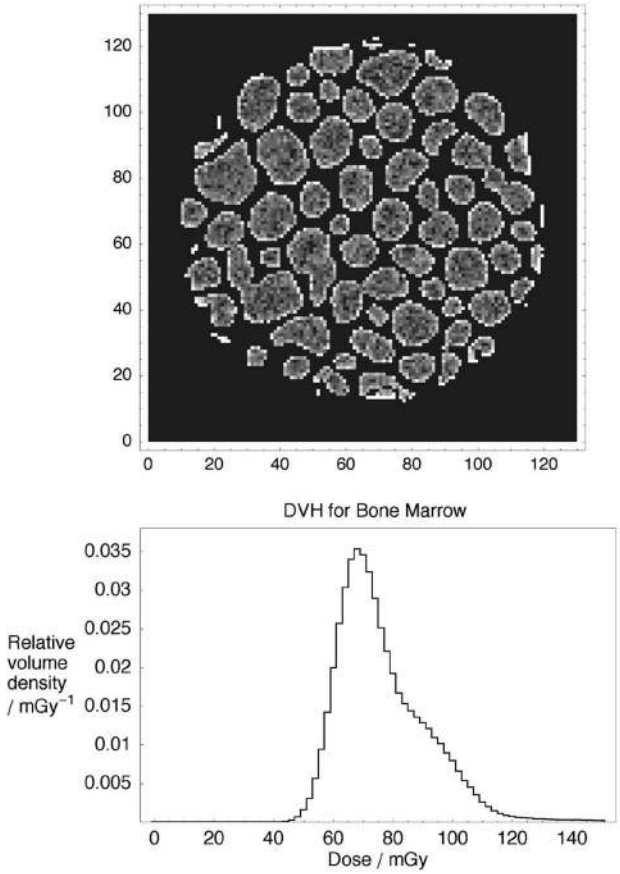


**Fig. 6.**

Dose in the bone phantom for a 80 kVp/3 mm Al beam: (a) cross section of the spatial dose distribution in bone marrow in the high resolution bone phantom, and (b) differential dose-volume histogram for the bone marrow.

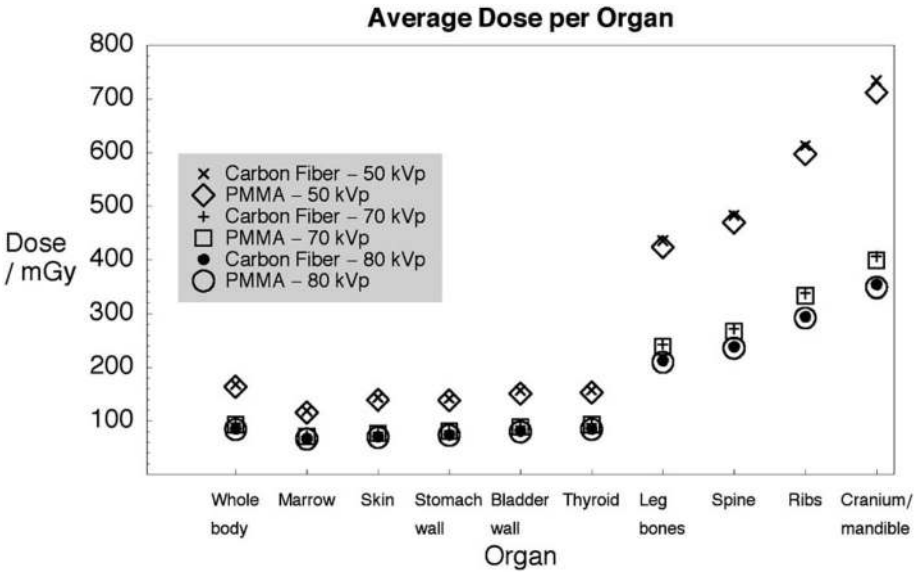


**Fig. 7.**
Average dose (for selected organs) for three beams and two mouse holders.

**Table I**

List of organs and tissue composition designation.

| Structure name | Composition designation |
|---|---|
| Skin | ICRU 46 Skin Adult |
| Body mass | Mixture: 80% ICRU 46 Muscle Adult + 20% ICRU 46 adispose tissue adult # 2 |
| Bladder wall | ICRU 46 Urinary Bladder empty |
| Bladder contents | water |
| Spine(bone) | ICRU 46 Skeleton-vertebral column (D6, L3) |
| Spine (marrow) | ICRU 46 Skeleton red marrow |
| Lungs | ICRU 46 Lung Adult (healthy) inflated |
| Trachea | NIST air (DRY) |
| Intestine contents | Water |
| Cranium | ICRU 46 Skeleton-cranium |
| Ribs | ICRU 46 Skeleton-ribs (2nd, 6th) |
| Lower limbs | ICRU 46 Skeleton-femur Adult (30 years) |
| Blood pool | ICRU 46 Blood Adult |
| Heart | ICRU 46 Heart Adult (healthy) |
| Kidney | ICRU 46 Kidney Adult |
| Liver | ICRU 46 Liver Adult (healthy) |
| Pancreas | ICRU 46 Pancreas Adult |
| Spleen | ICRU 46 Spleen Adult |
| Intestine wall | ICRU 46 GI tract (intestine) Adult |
| Brain | ICRU 46 Brain (whole) Adult |
| Stomach wall | ICRU 46 average soft tissue Adult ICRU-33 (ICRU,1980) |
| Stomach contents | water |
| Vas deferens | ICRU 46 average soft tissue Adult ICRU-33 (ICRU,1980) |
| Testes | ICRU 46 Testis Adult |
| Thyroid | ICRU 46 Thyroid Adult |

## Table II

Calculated values for the estimation of the number of photons required by simulations according to the Monte Carlo and measurements method.

| | Beam peak voltage (kVp) | | |
|---|---|---|---|
| | **50** | **70** | **80** |
| Exposure reading ($\mu$C/kg air) | 7.38 | 6.34 | 6.26 |
| Measured dose in air (mGy) | 0.250 | 0.215 | 0.212 |
| Simulated dose in air for $10^9$ photons ($\mu$Gy) | 8.7 | 5.9 | 5.3 |
| Calibration factor ($10^{11}$ photons/mA s) | 1.15 | 1.45 | 1.62 |
| Relative difference with line 5, Table III | 6% | 9% | 12% |

## Table III

Parameters and calculated values for the analytical estimation of the number of photons required by simulations.

| | Beam peak voltage (kVp) | | |
|---|---|---|---|
| | **50** | **70** | **80** |
| Exposure reading ($\mu$C/kg air) | 7.38 | 6.34 | 6.26 |
| Total energy deposit in chamber from Eq. (1) (GeV) | 5.8 | 4.975 | 4.91 |
| Photon flux from Eq. (2) ($\times 10^{11} sr^{-1} mA^{-1} s^{-1}$) | 6.78 | 8.16 | 8.75 |
| Average energy deposit per photon from Eq. (5) (eV) | 2.61 | 1.83 | 1.66 |
| Required number of photons for full field-of-view (0.16 s) at 1 mA s ($\times 10^{11}$) | 1.08 | 1.33 | 1.44 |
| Air density at 70 F, 1 atm, 60% R.H. ($kg/m^3$) | 1.2 | | |
| Average cord length through chamber (mm) | 4.28 | | |
| Solid angle subtended by the chamber (sr) | 0.013 | | |

## Table IV

Dose average and 95th percentile for the list of considered organs. Columns are: the total dose for a 90 mA s microCT examination, the relative dose expressed as mGy per mGy air kerma at the isocenter (21.8 cm), and the ratio of the 95th percentile of the dose distribution over the average. Data apply to the 70 kVp/2 mm Al beam with the mouse positioned in the custom PMMA bed.

| | Average | | |
|---|---|---|---|
| **Structure name** | **90 mAs microCAT II (mGy)** | **(mGy/mGy kerma)** | **Ratio 95th percentile/average** |
| Spine (marrow) | 71 | 0.9 | 1.10 |
| Vas deferens | 74 | 1.0 | 1.12 |
| Skin | 76 | 1.0 | 1.19 |
| Body mass | 79 | 1.0 | 1.13 |
| Stomach wall | 80 | 1.0 | 1.12 |
| Testes | 80 | 1.0 | 1.11 |
| Pancreas | 84 | 1.1 | 1.11 |
| Intestine wall | 85 | 1.1 | 1.11 |
| Heart | 85 | 1.1 | 1.10 |
| Brain | 86 | 1.1 | 1.10 |
| Liver | 87 | 1.1 | 1.10 |
| Lungs | 88 | 1.1 | 1.16 |
| Bladder wall | 88 | 1.1 | 1.12 |
| Kidney | 89 | 1.1 | 1.10 |
| Spleen | 92 | 1.2 | 1.08 |
| Thyroid | 92 | 1.2 | 1.09 |
| Whole body | 93 | 1.2 | 2.88 |
| Lower limbs | 238 | 3.1 | 1.36 |
| Spine (bone) | 267 | 3.4 | 1.16 |
| Ribs | 333 | 4.3 | 1.07 |
| Cranium | 398 | 5.1 | 1.09 |